Ultra-Narrow Depletion Layers in a Hematite Mesocrystal-Based Photoanode for Boosting Multihole Water Oxidation

Zhang, Zhujun

Nagashima, Hiroki

Tachikawa, Takashi

(Citation)
Angewandte Chemie International Edition,59(23):9047-9054

(Issue Date)
2020-06-02

(Resource Type)
journal article

(Version)
Accepted Manuscript

RESEARCH ARTICLE

Ultra-Narrow Depletion Layers in Hematite Mesocrystal-Based Photoanode for Boosting Multihole Water Oxidation

Zhujun Zhang, Hiroki Nagashima, and Takashi Tachikawa*

[*] Z. Zhang
Department of Chemistry, Graduate School of Science
Kobe University
1-1 Rokkodai-cho, Nada-ku, Kobe 657-8501 (Japan)
Dr. H. Nagashima, Prof. T. Tachikawa
Molecular Photoscience Research Center
Kobe University
1-1 Rokkodai-cho, Nada-ku, Kobe 657-8501 (Japan)
Email: tachikawa@port.kobe-u.ac.jp

(Present address) Dr. H. Nagashima
Department of Chemistry, Graduate School of Science and Engineering
Saitama University
255 Shimo-Okubo, Sakuraku, Saitama 338−8570, (Japan)

Supporting information for this article is given via a link at the end of the document.

Abstract: Significant charge recombination that is difficult to suppress limits the practical applications of hematite (α-Fe_2O_3) for photoelectrochemical water splitting. In this study, Ti-modified hematite mesocrystal superstructures assembled from highly oriented tiny nanoparticle (NP) subunits with sizes of ~5 nm were developed to achieve the highest photocurrent density (4.3 mA cm^{-2} at 1.23 V vs. RHE) ever reported for hematite-based photoanodes under back illumination. Due to rich interfacial oxygen vacancies yielding an exceedingly high carrier density of 4.1 × 10^{21} cm^{-3} for super bulk conductivity in the electrode and a large proportion of ultra-narrow depletion layers (<1 nm) inside the mesoporous film for significantly improved hole collection efficiency, a boosting of multihole water oxidation with very low activation energy (E_a = 44 meV) was realized.

Introduction

Photoelectrochemical (PEC) water splitting allows for the direct conversion of solar energy to clean and renewable energy sources such as H_2 gas, providing an attractive solution to issues such as fossil fuel depletion and CO_2 emissions.[1] Recently, various types of semiconductors, such as oxynitrides (e.g., $BaTaO_2N$),[2] nitrides (e.g., Ta_3N_5),[3] and oxyfluorides (e.g., $Pd_2TiO_{5.4}F_{1.2}$),[4] were developed as photoanode materials for visible-light water oxidation with high activity, but most of them suffer from the problems of low stability and high cost. The development of semiconductor electrodes for PEC water oxidation that are efficient, economically viable, and long-term recyclable is therefore still challenging.[5] As one of the most abundant metal oxides, the semiconductor hematite (α-Fe_2O_3) is a promising candidate for photoanodes owing to its suitable bandgap (~2.1 eV) for sunlight absorption, low cost, and long-term stability in alkaline aqueous solutions.[6] During the past decade, the development of efficient hematite photoanodes possessing high photocurrent densities with sufficiently cathodic onset potentials has attracted significant attention, but there has not been commensurate progress in this area.[7] Hematite has several performance-limiting characteristics, including poor carrier mobility (~10^{-2} cm^2 V^{-1} s^{-1}) and short minority carrier lifetime (picosecond time scale), leading to the occurrence of considerable bulk/surface recombination.[6] Nanostructuring of semiconductors has been thus employed to suppress such recombination by shortening the hole diffusion length to the surface.[8] While this approach has demonstrated successful outcomes such as the construction of nanostructured thin films,[8] it does not address the fundamental issue of a short diffusion length giving rise to poor light harvesting ability (α^{-1} = 0.12 μm at 550 nm, where α is the absorption coefficient for hematite).[6] Sluggish water oxidation kinetics (first-order reaction pathway) is another serious problem hindering the improvement of the PEC performance of hematite-based photoanodes.[6] As revealed by transient absorption measurements, operando spectroelectrochemistry, and density functional theory (DFT) studies conducted by Durrant at al., hematite follows third-order reaction kinetics when the surface hole density is high enough to oxidize the nearest neighboring metal atoms to form Fe(OH)-O-Fe(OH) sites.[9] This finding suggests that improving the hole collection efficiency is a potential solution for optimizing the surface water oxidation kinetics.

Metal oxide mesocrystals (MCs) are superstructures constructed from highly ordered nanoparticle (NP) subunits with tunable optical, electronic, and magnetic properties, and show great promise for applications ranging from catalysis to optoelectronics.[10] Interfacing between attached NPs inside the MC particles produces highly ordered structures, allowing for much higher crystal-to-crystal charge transfer efficiency compared to randomly aggregated NP systems.[11] Moreover, we have recently demonstrated the presence of interfacial oxygen vacancies (V_Os) created via fusion of the unique interfaces between the attached NP subunits inside hematite MCs.[12] The formation of interfacial V_Os has also been reported for other metal oxides such as Ni-doped SnO_2.[13] Unlike V_Os on the surface, which might act as recombination centers,[14] bulk V_Os are able to

serve as donor centers and, thus, significantly improve the bulk conductivity.[12] These findings show that proper engineering of the location and concentration of the V_Os might positively modify the PEC behaviors of hematite, but very limited attention has been paid so far.

Herein, we demonstrated that increasing the concentration of interfacial V_Os by decreasing the size of primary NPs inside MCs down to ~5 nm considerably improved the PEC performance of hematite-based photoanodes to achieve the highest photocurrent density (4.3 mA cm^{-2} at 1.23 V vs. RHE) under back illumination. The rich of interfacial V_Os in the bulk, formed via fusion of the interfaces between the attached tiny NPs inside the MCs during thermal annealing in air, resulted in an exceedingly high carrier density (N_d) of 4.1 × 10^{21} cm^{-3}, providing excellent bulk conductivity, as revealed at the bulk and single-particle levels. This feature was also shown to largely improve the hole collection efficiency by formation of ultra-narrow depletion layers (<1 nm) at the hematite/electrolyte interface, enabling a third-order water oxidation kinetic with an ultra-low activation energy (E_a) of 44 meV.

Results and Discussion

Fe_2O_3(Ti) MCs with tiny NP subunits were synthesized by a surfactant-free solvothermal method (Figure 1a). In a typical sample preparation, an ethanol/water solvent mixture containing $Fe(acac)_3$ and TiF_4 at a molar ratio of 10/1 in a well-sealed stainless-steel autoclave was heated at 453 K for a set amount of time. Fe_2O_3(Ti) single crystals (SCs) with diameters of several nanometers were formed by nucleation during the first 4 h (Figure S1). After 13 h, these primary Fe_2O_3(Ti) SCs self-assembled to form Fe_2O_3(Ti) MCs with a specific preferable mutual orientation to lower the surface energy.[15] The assembled tiny NP subunits inside the MCs were allowed to grow further via crystallographic fusion (Figure S2).[15a]

A representative sample of Fe_2O_3(Ti) MCs synthesized by solvothermal treatment for 13 h displayed a spherical morphology with diameters ranging from 80 to 150 nm as revealed by field-emission scanning electron microscopy (FE-SEM) (Figure S2a,b) and transmission electron microscopy (TEM) (Figures 1b and S1c). The Fe_2O_3(Ti) MCs were assembled from closely attached smaller NPs (~5 nm in size). Due to particle-to-particle interactions, the tiny NPs assembled in the MCs were crystallographically aligned, as indicated by single-crystal-like diffraction spots visible in the selective area electron diffraction (SAED) pattern (Figure 1b, inset) collected from the entire region of the MC. The diffraction spots were assigned to the (006), (113), and (110) planes of hematite along the [$2\bar{1}0$] zone axis.[16] High-angle annular dark-field scanning transmission electron microscopy (HAADF-STEM) in Figure 1e and energy-dispersive X-ray spectroscopy (EDX) elemental mapping images given in Figure 1f indicate uniform dispersion of Fe, O, and Ti ions in the MC particles. The corresponding EDX spectra (Figure S3) exhibited an Fe/Ti atomic ratio of approximately 92/8, which is close to the molar ratio of the metal precursors. There was almost no change in the sizes of the Fe_2O_3(Ti) MCs with longer solvothermal treatment times (24 and 48 h), but larger NP subunits with sizes ranging from ~13 to 20 nm were observed due to crystallographic fusion of tiny NPs inside the Fe_2O_3(Ti) MCs (Figure 1c and d). The surface black regions observed in Figures 1b-d for the as-synthesized Fe_2O_3(Ti) MCs are possibly due to residual acac groups from the iron precursors, which can be totally removed by annealing at temperatures above 773 K.[15a] Additionally, single-crystal-like diffraction spots of ($\bar{2}$10), ($\bar{1}$20), and (110) planes along the [001] zone axis were detected for these samples, indicating that crystallographic fusion of the highly oriented tiny NPs did not alter their single-crystal nature but slightly changed their orientation (Figures 1c and d, inset). Powder X-ray diffraction (XRD) patterns of the samples (Figure 1g) exhibited 2-theta peaks at 24.15, 33.10, 35.60, 40.85, 49.45, and 54.1°, which showed good agreement with a standard Powder Diffraction File (PDF) card of hematite (PDF#33-0664). The peak intensity of the (104) face was found to gradually increase with the solvothermal treatment time, consistent with the evolution of the crystal orientation observed from the SAED patterns. This suggested that increasing the degree of crystallinity of hematite by increasing the solvothermal treatment time or temperature led to a preference for the (104) face, and this observation has also been reported elsewhere.[17] The grain sizes estimated from the line broadening of the main diffraction peak (104) or (110) using the Scherrer equation were almost identical to the NP sizes estimated from TEM images. The absence of Ti peaks was likely due to the low concentration of Ti ions uniformly dispersed in the MC, as evident in the elemental map shown in Figure 1f.

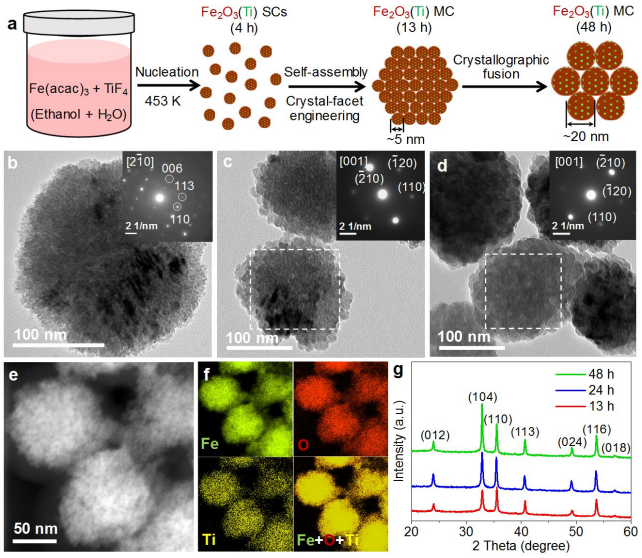

Figure 1. (a) Schematic illustration of the synthesis of Fe_2O_3(Ti) MCs assembled with different sizes of NP subunits. TEM (inset: corresponding SAED pattern) images of Fe_2O_3(Ti) MCs synthesized under solvothermal treatment for 13 h (b), 24 h (c), 48 h (d), respectively. HAADF-STEM (e) and corresponding EDX element mapping images (f) of the Fe_2O_3(Ti) MCs synthesized under solvothermal treatment for 13 h. (g) XRD patterns of the Fe_2O_3(Ti) MCs synthesized under solvothermal treatment for different times.

The photoanodes were fabricated by a multiple spin-coating method as we reported recently.[12] All prepared photoanodes were annealed prior to PEC measurements at 973 K for 20 min in air. The thermally treated sample is hereafter referred to as Fe_2O_3(Ti) MC_T. The sintering process produced an abundance of inner mesopores with diameters ranging from 10 to 25 nm inside particles (Figure 2a), as seen in the cross-sectional FE-SEM (Figure 2b), TEM (Figure S4a), and HAADF-STEM images

(Figure S4b). Open pore windows are clearly visible in the FE-SEM image (Figure S4c), which enable electrolytes to infiltrate the inner mesopores and, thus, establish a semiconductor-electrolyte junction (i.e., band bending) for charge separation. This could allow for the creation of a large number of depletion regions on both the outer and inner pore surfaces, which would lead to a significant decrease in the hole drift distance and simultaneous increase in the hole collection pathway. Furthermore, these open windows in the inner mesopores would improve the light absorption efficiency through light scattering or transmission, allowing for a greater number of hematite MCs to be excited.

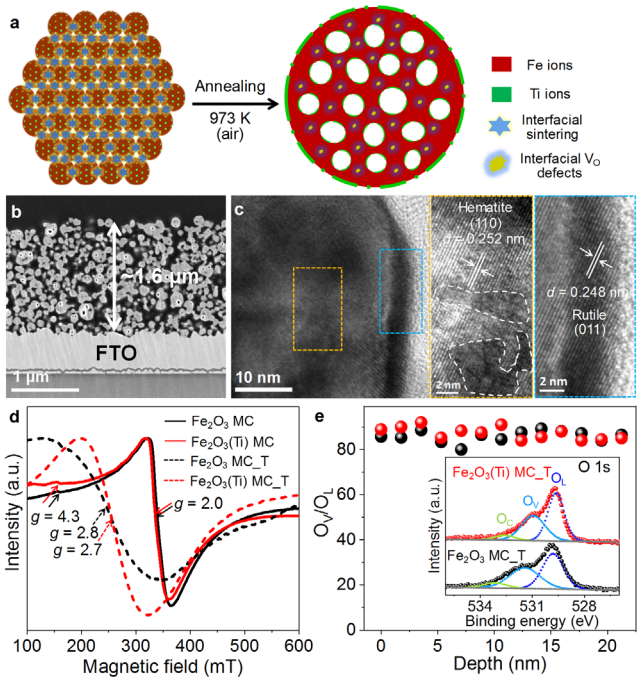

Figure 2. (a) Schematic illustration of the formation of single-crystal mesoporous hematite with a thin TiO_2 overlayer and interfacial V_O defects in the bulk. (b) Cross-sectional FE-SEM image of the optimized Fe_2O_3(Ti) MC_T photoanode. (c) HRTEM images of typical Fe_2O_3(Ti) MC_T particles collected after annealing at 973 K for 20 min in air. (d) EPR spectra of the samples. (e) The area ratios of O_V/O_L for different depths of Fe_2O_3 MC_T (black) and Fe_2O_3(Ti) MC_T (red) samples estimated from their O 1s XPS depth profiles given in Figure S7. The inset shows typical O 1s XPS spectra of the samples.

An optimized photoanode with a film thickness of ~1.6 μm was constructed from attached mesoporous Fe_2O_3(Ti) MC_T particles (Figure 2b). The size of the Fe_2O_3(Ti) MC_T particles was well matched with the surface roughness of the fluorine doped tin oxide (FTO) substrate, allowing for optimum electric contact. The single-crystal nature of the Fe_2O_3(Ti) MC_T sample was not altered by high temperature annealing, as evidenced by single-crystal-like diffraction spots in the SAED pattern (Figure S4a, inset). Evolution of the crystal orientation determined from SAED patterns of the samples before and after annealing (insets of Figures 1a and S4a) showed that the (104) face was thermally preferable. Figure 2c shows corresponding high-resolution TEM (HRTEM) images. The lattice spacing in the bulk region was 0.252 nm, which was assigned to the typical (110) crystal plane of hematite. Distorted fringes (e.g., regions surrounded by white dotted lines) can be observed in the bulk region, suggesting the formation of lattice defects. According to our previous study,[12] thermal sintering of highly ordered interfaces between attached NP subunits inside the MC induces surface reconstruction at the interfaces (i.e., formation of interfacial V_Os) as illustrated in Figure 2a. A high degree of contrast between the surface and bulk regions suggested the formation of a thin overlayer (<1–3 nm) on the surface. The lattice spacing in this overlayer region was 0.248 nm, indicative of the formation of rutile TiO_2 with a (011) plane.

The inner compositions of the samples were also analyzed by X-ray photoelectron spectroscopy (XPS) depth profiles (Figure S5), which showed no variation in the atomic concentration of Ti(Fe) ions between the surface and bulk regions (~20 nm) for the as-synthesized Fe_2O_3(Ti) MCs, which was also consistent with EDX elemental mapping (Figure1f). Following thermal treatment, the atomic percentages of Ti (Fe) ions were higher (lower) at the surface region (~3 nm) than that at the bulk region, suggesting that Ti ions were mostly segregated from the ions in the bulk. The crystal phase evolution was also confirmed by XRD analysis (Figure S6). In addition to the diffraction peaks of hematite, a new 2-theta diffraction peak at 27.5° was detected for all Fe_2O_3(Ti) MC_T samples after thermal treatment, and assigned to the (110) plane of rutile phase TiO_2.[12] These results confirmed that the observed thin overlayer on the surface (Figure 2c) was rutile TiO_2. Furthermore, the peak intensity of the (104) face significantly increased after thermal treatment, also confirming thermal preference of the (104) face due to an increase in the degree of crystallinity of hematite.

To confirm the formation of an abundance of V_Os in the MCs, electron paramagnetic resonance (EPR) and O 1s XPS measurements were performed (Figures 2d, e, and S7). As-synthesized Fe_2O_3 and Fe_2O_3(Ti) MCs exhibited two main signals at g = 2.0 (Fe^{3+} ions coupled via exchange interactions) and 4.3 (Fe^{3+} ions in rhombic and axial symmetry sites), respectively, indicating that no Fe^{2+} (i.e., V_Os) was formed in the samples. After annealing, however, the lineshapes evolved to single broad resonance lines with signals centered at g = 2.8 and 2.7 for Fe_2O_3 MC_T and Fe_2O_3(Ti) MC_T, respectively. The changes in line shapes indicate the occurrence of a ferromagnetic resonance due to the interaction between Fe^{2+} and Fe^{3+}.[18,19] For the O 1s XPS spectra (inset of Figure 2e), peaks with binding energies at approximately 530.2, 531.9, and 533.3 eV were assigned to lattice O^{2-} species (O_L), iron-oxygen species near V_Os (O_V), and chemisorbed or dissociated oxygen species from the H_2O molecules (O_C), respectively.[20] Both the Fe_2O_3 MC_T and Fe_2O_3(Ti) MC_T samples exhibited high O_V concentrations, indicating formation of an abundance of V_Os. The O 1s XPS depth profiles (Figure 2e and S7) show that the peak area ratio O_V/O_L remained almost unchanged between the surface and bulk regions (~20 nm) for both the MC samples, implying that the abundance of V_Os in the bulk was created not only by diffusion of Ti ions, but also by sintering of the interfaces between the highly oriented NP subunits that occurred during thermal treatment (Figure 2a). A similar phenomenon was observed for a sample with larger NP subunits synthesized by a different method.[12]

The charge transfer efficiencies of the Fe_2O_3(Ti) MC_T photoanodes with different sizes of NP subunits were firstly analyzed by electrochemical impedance spectroscopy (EIS) (Figure 3a). EIS curves were fitted using the equivalent circuit model (Figure S8) and all simulated parameters are summarized in Table S1. The electron transfer resistances both in the bulk (R_{ct}) and at the interfaces of hematite/FTO (R_s) and hematite/electrolyte (R_{trap}) decreased with the decrease of particle

size. In addition, all the Fe_2O_3(Ti) MC_T photoanodes gave much lower R values than those of the unmodified Fe_2O_3 MC_T photoanode (Figure S9, Table S1), indicating that the Ti-modification significantly improved the charge transfer efficiency.[21] Particularly, a super bulk conductivity was realized by the optimized Fe_2O_3(Ti) MC_T as indicated by its ultra-low R_{ct} (10 Ω cm^{-2}). The higher charge transfer efficiency of the Fe_2O_3(Ti) MC_T with smaller size of NP subunits was attributed to its greatly enhanced carrier density (N_d) calculated from the slope of the Mott-Schottky plot given in Figure 3b (see Eq S1). The optimized sample showed a N_d of 4.1 × 10^{21} cm^{-3}, which is much higher than the highest carrier density ever obtained by element-doped or modified hematite electrodes (with a magnitude of 10^{20} cm^{-3}). The significantly enhanced carrier density was attributed to the formation of an abundance of interfacial V_Os in the bulk, as verified by the O 1s XPS depth profile (Figure S10), which can serve as donor centers to improve the bulk conductivity.[22]

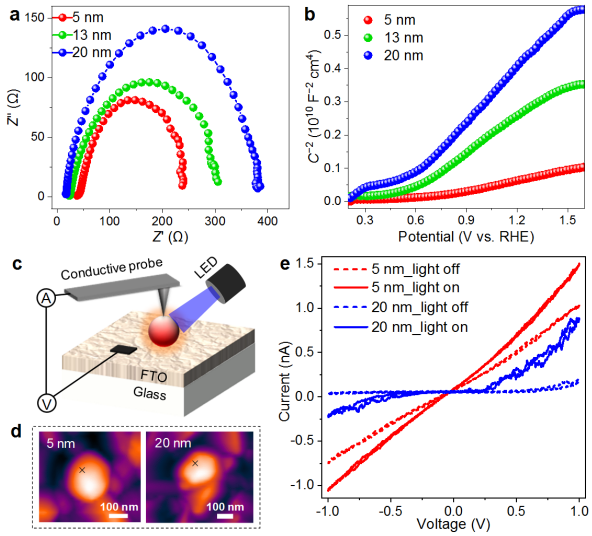

Figure 3. (a) EIS and (b) Mott-Schottky plots of the samples. (c) Schematic illustration of the pc-AFM measurements. (d) AFM images of a single Fe_2O_3(Ti) MC_T particle with NP subunits with smaller (left) and larger sizes (right). The cross marks indicate the measured locations. (e) The corresponding current-potential curves of a single Fe_2O_3(Ti) MC_T particle with different sizes of NP subunits.

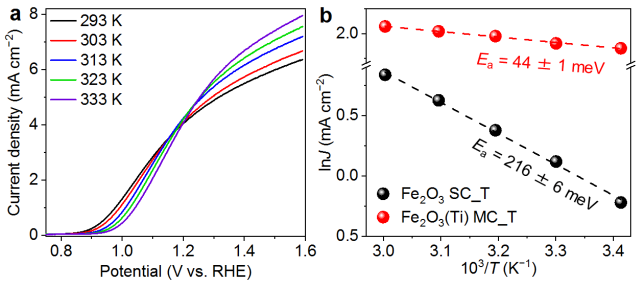

Figure 4. (a) Current density-potential curves of the optimized Fe_2O_3(Ti) MC_T photoanode measured in 1.0 M NaOH electrolyte at different temperatures. (b) Arrhenius plots of ln$J$ vs. 1/T at 1.6 V vs. RHE obtained for the optimized Fe_2O_3(Ti) MC_T and Fe_2O_3 SC_T systems.

Although electrochemical measurements can macroscopically analyze the properties of photoanodes, the nanoscopic variations within the electrode or single particle are still not able to be determined by such ensemble experiments. We thus employed photoconductive atomic force microscopy (pc-AFM)[23,24] to elucidate structure-correlated electrical transport properties inherent in individual MC particles with nanoscale resolution (Figures 3c-e, S11). Bias potentials ranging from −1.0 to 1.0 V were applied to the sample using a Ti/Ir-coated conductive probe with a 25 nm tip radius, and the current was simultaneously collected under dark conditions or light irradiation in an N_2 atmosphere. AFM topological images of Fe_2O_3(Ti) MC_T with smaller (5 nm) and larger (20 nm) NP subunits are shown in Figure 3d, respectively. The current-potential curves (Figure 3e) of a Fe_2O_3(Ti) MC_T particle with smaller NP subunits (~5 nm) exhibited a linear shape, indicating a typical bulk-limited transport (Poole-Frenkel emission) process where the bulk defects dominate the electric conduction.[25] For comparison, a Fe_2O_3(Ti) MC_T particle with larger NP subunits (~20 nm) showed a current onset (>0.25 V) in the low potential region (Figure 3e) due to Schottky contact. Schottky emission is an interface-limited conduction that occurs at low voltages, whereby electrons transit above the potential barrier on the surface of a semiconductor.[24] Both the Poole–Frenkel and Schottky emissions originate from lowering of the Coulombic potential barrier for free-charge generation out of defect centers or trap sites under a bias potential.[24] The linear shape of the current-potential curves of the Fe_2O_3(Ti) MC_T particle with smaller NP subunits thus indicated facile charge transfer occurring as a consequence of a higher N_d value created by higher V_O levels in the bulk. These results confirmed that a higher concentration of interfacial V_Os can be created inside the bulk of individual hematite MCs with smaller NP subunits, producing a large increase in the conductivity for optimum solar water splitting activity.

To unravel the water oxidation mechanism, the temperature dependence of photocurrent generation from the optimized Fe_2O_3(Ti) MC_T photoanode was studied (Figure 4a). Upon increasing the temperature from 293 to 333 K, the Fe_2O_3(Ti) MC_T photoanode exhibited an increase in the photocurrent at 1.6 V vs. RHE from 6.4 to 8.0 mA cm^{-2}. The onset potential gradually shifted from 0.8 (293 K) to 0.9 V (333 K) vs. RHE in terms of enhanced surface charge recombination (Figures S12, S13) as reported for porous Mo:$BiVO_4$ and rutile TiO_2.[26] Typically, hematite following a first-order water oxidation mechanism with a large activation barrier in the order of 0.2–0.7 eV.[9,27] However, the activation energy obtained from Arrhenius-type plots of ln$J$ vs. 1/T at 1.6 V vs. RHE for the Fe_2O_3(Ti) MC_T system was only 44 ± 1 meV (Figure 4b), which was better agreement with the third-order water oxidation mechanism than with first-order kinetics, i.e., a multihole water oxidation pathway was present in MCs at room temperature under the irradiation of one sun. As a result of much higher N_d (4.1 × 10^{21} cm^{-3}) and charge separation efficiency for a better surface hole accumulation, a significant decrease of ~172 meV in activation energy can be realized when compared to a reference sample constructed from randomly aggregated hematite single crystals (Fe_2O_3 SC_T, 216 ± 6 meV, first-order kinetics) with a much lower carrier density (2.4 × 10^{19} cm^{-3})[12] (Figures 4b and S14).

An optimum film thickness of ~1.6 μm was chosen by comparing the photocurrent densities at 1.23 V vs. RHE for Fe_2O_3(Ti) MC_T photoanodes prepared with different numbers of

spin-coating cycles under back and front illumination (Figure S15). Because electron transport from the excited regions to the FTO is limited by a trapping process,[12] back illumination provides a higher photocurrent density than front illumination, especially in films with thicknesses greater than the optical penetration depth (~900 nm based on our previous study[12]). Figure 5a compares the PEC performance of the prepared photoanodes under back illumination. The Fe_2O_3(Ti) MC_T experienced a tremendous increase in the photocurrent density compared to the unmodified Fe_2O_3 MC_T, indicating superior charge separation and transfer due to Ti-modification. For the Fe_2O_3(Ti) MC_T with different size of NP subunits, the photocurrent densities increased in the order of 20 nm (2.7 mA cm^{-2}) < 13 nm (3.5 mA cm^{-2}) < 5 nm (4.3 mA cm^{-2}) at 1.23 V vs. RHE. The photocurrent density at 1.23 V vs. RHE for the optimized Fe_2O_3(Ti) MC_T (4.3 mA cm^{-2}) was three times that of the Fe_2O_3 MC_T (1.5 mA cm^{-2}). To the best of our knowledge, this is the highest value reported thus far for hematite-based photoanodes under back illumination (Table S2). Back illumination is beneficial for cell operation since light scattering or shadowing by evolved gas bubbles is relatively small. Following deposition of a cobalt-phosphate (Co-Pi) oxygen evolution co-catalyst on the surface of Fe_2O_3(Ti) MC_T via photo-assisted deposition (Figure S16),[28] the photocurrent density further increased to 5.5 mA cm^{-2} at 1.23 V vs. RHE and the onset potential showed a cathodic shift from 0.8 to 0.6 V vs. RHE. The significant onset potential shift of 0.2 V as well as the increase of the photocurrent density clearly indicated effective suppression of surface charge recombination.[28] The current-to-fuel conversion efficiency was quantitatively evaluated by detecting the gaseous products via gas chromatography. As shown in Figure S17, the production of both H_2 and O_2 gasses was linear with respect to the irradiation time, with a stoichiometric ratio of 2:1 and Faradaic efficiencies (FEs) over 95%.

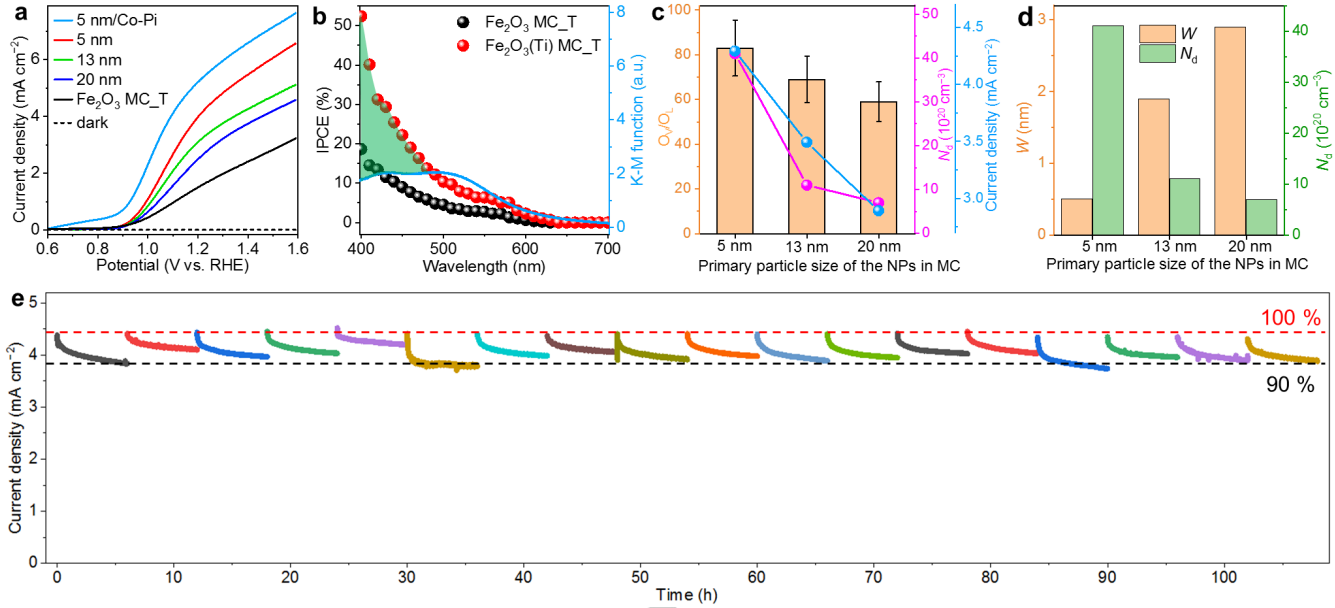

Figure 5. (a) Current density-potential curves of the samples. 20, 13, 5 nm represents the Fe_2O_3(Ti) MC_T photoanodes with the primary particle size of the NPs in MC. (b) IPCE curves measured at 1.23 V vs. RHE for Fe_2O_3 MC_T and Fe_2O_3(Ti) MC_T photoanodes. The steady-state UV-visible diffuse reflectance spectrum of the Fe_2O_3(Ti) MC_T is shown as a Kubelka-Munk function for comparison. (c) The relationships between the sizes of the NP subunits inside Fe_2O_3(Ti) MCs and peak area ratio O_V/O_L of the samples estimated from O 1s XPS depth profiles given in Figure S10, carrier density (N_d), and photocurrent densities at 1.23 V vs. RHE. (d) The relationship between the depletion width (W), size of primary NPs in the MC, and N_d. (e) Durability and recyclability tests of the optimized Fe_2O_3(Ti) MC_T photoanode.

Incident photon-to-current conversion efficiencies (IPCEs) (see Eq S2) were also measured at 1.23 V vs. RHE under back illumination using monochromatic light with different wavelengths (Figure 5b). Excellent IPCEs were observed throughout the entire wavelength range (400–620 nm) for the optimized Fe_2O_3(Ti) MC_T photoanode. At 400 nm, the IPCE was ~53% for the Fe_2O_3(Ti) MC_T photoanode, which was three times higher than that for Fe_2O_3 MC_T (18%). For comparison, the steady-state UV-visible diffuse reflectance spectrum of Fe_2O_3(Ti) MC_T is shown in Figure 5b. There was no apparent change in the light absorption efficiency in the shorter wavelength range of 400–500 nm, even though the IPCEs of the MC-based photoanodes were much higher in this region. With longer excitation wavelengths (500–620 nm), the magnitudes of the IPCE spectra followed the changes in light absorption efficiencies. The temperature-dependent photocurrent generation under excitation with light sources of different wavelengths was investigated (Figure S18). As summarized in Figure S18c, it is clear that the activation energy (34 ± 1 meV) obtained by excitation with light of a short wavelength (430 nm) was much lower than that (68 ± 1 meV) obtained by excitation with light of a longer wavelength (530 nm). This finding suggested that holes with a long lifetime (likely shallowly trapped O^- holes) produced by short wavelength light excitation of MCs with an abundance of interfacial V_Os would contribute to hole accumulation and subsequently acceleration of the water oxidation kinetics. Such long-lived holes can efficiently transport to the hematite/electrolyte interfaces, thus resulting in largely enhanced photocurrent generation.

For practical utilization, PEC systems should provide not only high solar-to-hydrogen efficiency at low cost, but also long-term

device durability. To simulate conditions in a natural environment, the current density-time curve of the optimized Fe_2O_3(Ti) MC_T photoanode was measured at 1.23 V vs. RHE under back illumination for 6 h (comparable to daytime sunlight), followed by the application of a 12 h dark cycle (comparable to night-time conditions). These measurements were repeated 18 times to evaluate the durability and recyclability. Despite there being a slight decrease of the photocurrent during illumination for 6 h, especially during first hour, the photocurrent recovered to its initial level in the following cycles of the durability test. Following completion of 18 cycles with a total illumination time of over 100 h, the photocurrent density was still 90% higher than that during the initial performance (Figure 5e), indicating that the present system possessed excellent durability and recyclability. The slight photocurrent loss, especially at the initial illumination stage, was likely due to the positive shift of the onset potential occurring as a result of the temperature increase (Figure S19). When the solution was stirred, the positive onset shift and increase of the electrolyte temperature were both suppressed, suggesting that the local temperature near the hematite surface was much higher than that of the electrolyte during initial illumination, thus leading to the positive shift of the onset potential and loss of photocurrent.

The enhanced PEC performance in the sample with smaller NP subunits was attributed to its higher N_d (Figures 3b, 5c, and S9b, Table S1). As the concentration of Ti ions was the same for all samples, the increase in N_d would originate from the higher concentration of interfacial V_Os in the sample with smaller NP subunits (Figure S10). The relationships between the sizes of the NP subunits inside the Fe_2O_3(Ti) MC, the peak area ratio O_V/O_L, N_d, and the photocurrent densities at 1.23 V vs. RHE are summarized in Figure 5c. It is apparent that the Fe_2O_3(Ti) MC_T photoanode with smaller NP subunits possessed a higher concentration of V_Os, thus contributing to a higher N_d and photocurrent density.

The occurrence of band bending in the depletion region with a width of W (see Eq S3) at the semiconductor/electrolyte interface yields a driving force for the separation of photogenerated charge carriers.[6] Charge recombination occurs within a distance beyond the sum of W and the minority carrier diffusion length L_D.[29] In the case of hematite, significant recombination occurs even in the electric field of the depletion region due to its L_D (2–4 nm) being small compared to typically reported depletion layer widths (~10 nm).[6] To suppress recombination, the hole migration distance for surface reactions should therefore be as small as possible. Due to its exceedingly high N_D (4.1×10^{21} cm^{-3}), Fe_2O_3(Ti) MC_T had a calculated W value of only ~0.5 nm. It should be noted that such ultra-narrow (<1 nm) depletion layers are rarely reported in the literature (e.g., Sn:In_2O_3 nanocrystals).[30] The relationships between the W, particle size, and N_d are illustrated in Figure 5d. Samples with larger NP sizes in the MC had relatively lower concentrations of interfacial V_Os in the bulk, resulting in relatively lower N_d and higher W values. With a higher W, the extent of charge recombination was greater due to the increased hole migration distance, and the resulting lower surface hole density lead to slower water oxidation kinetics (Figure S20).

The deep band bending on the surface should provide a great enough potential gradient to drive the separation of photogenerated electrons and holes (Scheme 1) and, thus, effectively suppress bulk recombination, as evidenced by the very small R_{ct} value (Table S1). In the mesoporous film with open pore windows, electrolyte can infiltrate to the pores and largely increase the proportion of semiconductor/electrolyte interfaces. Accordingly, a large proportion of ultra-narrow depletion regions (<1 nm) were created on both the outer surfaces and inner pore surfaces of the MC particles, resulting in an increase in surface hole accumulation for the equilibrium between three surface holes and the triply oxidized cluster (Fe(OH)-O-Fe(OH)) after O-O bond formation (the rate determining step),[9] and thus finally realize a efficient multihole water oxidation kinetics with almost no activation barrier (Figure 4).

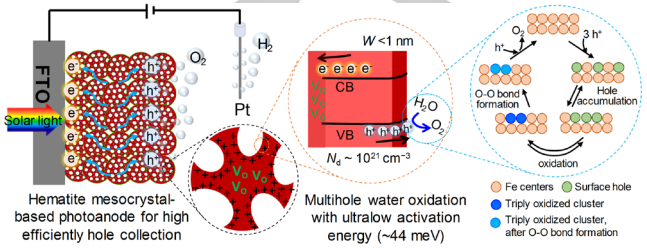

Scheme 1. Schematic illustration of charge carrier dynamics in the hematite MC-based photoanode with an abundance of bulk V_Os and third-order-like surface water oxidation kinetics.

Conclusion

In conclusion, we demonstrated that decreasing the sizes of primary NPs inside the MCs was an effective route towards increasing the concentration of interfacial V_Os in the bulk to yield an exceedingly high carrier density of 4.1×10^{21} cm^{-3}, giving excellent bulk conductivity as confirmed by pc-AFM measurements on single MC particles and producing a large quantity of ultra-narrow depletion regions (<1 nm), resulting in significantly improved hole collection efficiency for third-order-like water oxidation kinetics with ultra-low activation energy (E_a = 44 ± 1 meV). Consequently, the optimized photoanode exhibited the highest reported photocurrent density (4.3 mA cm^{-2} at 1.23 V vs. RHE) and good durability (over 100 h) for hematite-based photoanodes under back illumination. Our study provides an attractive alternative strategy based on interfacial defect engineering for improving the PEC performance of metal oxide semiconductors.

Acknowledgements

Prof. Yasuhiro Kobori (Kobe University) and Dr. Hiroaki Sugasawa (Oxford Instruments) are acknowledged for EPR and pc-AFM measurements, respectively. Kaneka Corporation is acknowledged for financial support. This work was partially supported by JST PRESTO Grant Number JPMJPR1316, JST A-STEP Grant Number AS3011905T, JSPS KAKENHI Grant Numbers JP18H01944, JP18H04517, and others. Zhujun Zhang thanks to the support from Marubun Research Promotion Foundation.

Keywords: Photoelectrochemical • multihole water oxidation • mesocrystals • oxygen vacancies • depletion layer

[1] a) A. Fujishima, K. Honda, *Nature* **1972**, *238*, 37–38; b) M. Grätzel, *Nature* **2001**, *414*, 338–344.

[2] S. Jeongsuk, M. Nakabayashi, T. Hisatomi, N. Shibata, T. Minegishi, K. Domen, *ACS Appl. Energy Mater.* **2019**, *2*, 5777–5784.

[3] T. Higashi, H. Nishiyama, Y. Suzuki, Y. Sasaki, T. Hisatomi, M. Katayama, T. Minegishi, K. Seki, T. Yamada, K. Domen, *Angew. Chem. Int. Ed.* **2019**, *58*, 2300–2304.

[4] N. Hirayama, H. Nakata, H. Wakayama, S. Nishioka, T. Kanazawa, R. Kamata, Y. Ebato, K. Kato, H. Kumagai, A. Yamakata, K. Oka, K. Maeda, *J. Am. Chem. Soc.* **2019**, *141*, 17158–17165.

[5] W. Yang, R. R. Prabhakar, J. Tan, S. D. Tilley, J. Moon, *Chem. Soc. Rev.* **2019**, *48*, 4979–5015.

[6] K. Sivula, F. L. Formal, M. Grätzel. *ChemSusChem* **2011**, *4*, 432-449.

[7] a) H. Zhang, J. H. Park, W. J. Byun, M. H. Song, J. S. Lee, *Chem. Sci.* **2019**, *10*, 10436–10444; b) H. Zhang, W. Y. Noh, F. Li, J. H. Kim, H. Y. Jeong, J. S. Lee, *Adv. Funct. Mater.* **2019**, *29*, 1805737; c) P.-Y. Tang, et al. *Adv. Energy Mater.* **2019**, *9*, 1901836; d) D. Cao, W. Luo, J. Feng, X. Zhao, Z. Li, Z. Zou, *Energy Environ. Sci.* **2014**, *7*, 752–759.

[8] a) S. Kment, F. Riboni, S. Pausova, L. Wang, L. Wang, H. Han, Z. Hubicka, J. Krysa, P. Schmuki, R. Zboril, *Chem. Soc. Rev.* **2017**, *46*, 3716–3769; b) C. Li, Z. Luo, T. Wang, J. Gong, *Adv. Mater.* **2018**, *30*, 1707502; c) D. A. Wheeler, G. Wang, Y. Ling, Y. Li, J. Z. Zhang, *Energy Environ. Sci.* **2012**, *5*, 6682–6702; d) H.-J. Ahn, A. Goswami, F. Riboni, S. Kment, A. Naldoni, S. Mohajernia, R. Zboril, P. Schmuki, *ChemSusChem* **2018**, *11*, 1873–1879; e) S. D. Tilley, M. Cornuz, K. Sivula, M. Grätzel. *Angew. Chem. Int. Ed.* **2010**, *49*, 6405–6408; f) H. Dotan, O. Kfir, E. Sharlin, O. Blank, M. Gross, I. Dumchin, G. Ankonina, A. Rothschild, *Nat. Mater.* **2013**, *12*, 158–164; g) S. C. Warren, K. Voïtchovsky, H. Dotan, C. M. Leroy, M. Cornuz, F. Stellacci, C. Hébert, A. Rothschild, M. Grätzel, *Nat. Mater.* **2013**, *12*, 842–849.

[9] a) C. A. Mesa, L. Francàs, K. R. Yang, P. Garrido-Barros, E. Pastor, Y. Ma, A. Kafizas, T. E. Rosser, M. T. Mayer, E. Reisner, M. Grätzel, V. S. Batista, J. R. Durrant, *Nat. Chem.* **2020**, *12*, 82–89; b) F. Le Formal, E. Pastor, S. D. Tilley, C. A. Mesa, S. R. Pendlebury, M. Grätzel, J. R. Durrant, *J. Am. Chem. Soc.* **2015**, *137*, 6629–6637.

[10] a) C. W. Wang, S. Yang, W. Q. Fang, P. Liu, H. Zhao, H. G. Yang, *Nano Lett.* **2016**, *16*, 427–433; b) T. Tachikawa, T. Majima, *NPG Asia Materials* **2014**, *6*, e100.

[11] a) P. Zhang, T. Tachikawa, M. Fujitsuka, T. Majima, *Chem. Eur. J.* **2018**, *24*, 6295–6307; b) Z. Bian, T. Tachikawa, P. Zhang, M. Fujitsuka, T. Majima, *Nat. Commun.* **2014**, *5*, 3038; c) T. Tachikawa, P. Zhang, Z. Bian, T. Majima, *J. Mater. Chem. A* **2014**, *2*, 3381–3388; d) P. Zhang, T. Tachikawa, M. Fujitsuka, T. Majima, *Chem. Commun.* **2015**, *51*, 7187–7190; e) Z. Bian, T. Tachikawa, P. Zhang, M. Fujitsuka, T. Majima, *J. Am. Chem. Soc.* **2014**, *136*, 458–465; f) P. Zhang, T. Tachikawa, M. Fujitsuka, T. Majima, *ChemSusChem* **2016**, *9*, 617–623; g) P. Zhang, T. Ochi, M. Fujitsuka, Y. Kobori, T. Majima, T. Tachikawa, *Angew. Chem. Int. Ed.* **2017**, *56*, 5299–5303.

[12] Z. Zhang, I. Karimata, H. Nagashima, S. Muto, K. Ohara, K. Sugimoto, T. Tachikawa, *Nat. Commun.* **2019**, *10*, 4832.

[13] P. I. Archer, P. V. Radovanovic, S. M. Heald, D. R. Gamelin, *J. Am. Chem. Soc.* **2005**, *127*, 14479–14487.

[14] Z. Wang, X. Mao, P. Chen, M. Xiao, S. A. Monny, S. Wang, M. Konarova, A. Du, L. Wang, *Angew. Chem. Int. Ed.* **2019**, *58*, 1030–1034.

[15] a) J. Cai, S. Chen, M. Ji, J. Hu, Y. Ma, L. Qi, *CrystEngComm* **2014**, *16*, 1553–1559; b) H. Wang, Q. Chen, Q. Luan, R. Duan, R. Guan, X. Cao, X. Hu, *Chem. Eur. J.* **2018**, *24*, 17105–17116.

[16] P. Li, X. Yan; Z. He, J. Ji, J. Hu, G. Li, K. Lian, W. Zhang, *CrystEngComm* **2016**, *18*, 1752–1759.

[17] S.-W. Cao, Y.-J. Zhu, *Nanoscale Res. Lett.* **2011**, *6*, 1.

[18] A. Jitianu, M. Crisan, A. Meghea, I. Rau, M. Zaharescu, *J. Mater. Chem.* **2002**, *12*, 1401–1407.

[19] M. M. Can, M. Coşkun, T. Firat, *J. Alloys. Comp.* **2012**, *542*, 241–247.

[20] E. McCafferty, J. P. Wightman, *Surf. Interface Anal.* **1998**, *26*, 549–564.

[21] a) T. Hisatomi, H. Dotan, M. Stefik, K. Sivula, A. Rothschild, M. Grätzel, N. Mathews, *Adv. Mater.* **2012**, *24*, 2699–2702; b) M. G. Ahmed, I. E. Kretschmer, T. A. Kandiel, A. Y. Ahmed, F. A. Rashwan, D. W. Bahnemann, *ACS Appl. Mater. Interfaces* **2015**, *7*, 24053–24062.

[22] a) Z. Zhou, J. Liu, R. Long, L. Li, L. Guo, O. V. Prezhdo, *J. Am. Chem. Soc.* **2017**, *139*, 6707–6717; b) S. Nishioka, J. Hyodo, J. J. M. Vequizo, S. Yamashita, H. Kumagai, K. Kimoto, A. Yamakata, Y. Yamazaki, K. Maeda, *ACS Catal.* **2018**, *8*, 7190–7200;.c) M. Sachs, J.-S. Park, E. Pastor, A. Kafizas, A. A. Wilson, L. Francàs, S. Gul, M. Ling, C. Blackman, J. Yano, A. Walsh, J. R. Durrant, *Chem. Sci.* **2019**, *10*, 5667–5677.

[23] F. A. L. Laskowski, S. Z. Oener, M. R. Nellist, A. M. Gordon, D. C. Bain, J. L. Fehrs, S. W. Boettcher, *Nat. Mater.* **2020**, *19*, 1–8.

[24] J. Eichhorn, C. Kastl, J. K. Cooper, D. Ziegler, A. M. Schwartzberg, I. D. Sharp, F. M. Toma, *Nat. Commun.* **2018**, *9*, 2597.

[25] J. P. Chang, Y.-S. Lin, *Appl. Phys. Lett.* **2001**, *79*, 3666–3668.

[26] L. Zhang, X. Ye, M. Boloor, A. Poletayev, N. A. Melosh, W. C. Chuec, *Energy Environ. Sci.* **2016**, *9*, 2044–2052.

[27] a) A. J. Cowan, C. J. Barnett, S. R. Pendlebury, M. Barroso, K. Sivula, M. Grätzel, J. R. Durrant, D. R. Klug, *J. Am. Chem. Soc.* **2011**, *133*, 10134–10140; b) E. Pastor, J.-S. Park, L. Steier, S. Kin, M. Grätzel, J. M. Durrant, A. Walsh, A. A. Bakulin, *Nat. Commun.* **2019**, *10*, 3962.

[28] D. K. Zhong, M. Cornuz, K. Sivula, M. Grätzel, D. R. Gamelin, *Energy Environ. Sci.* **2011**, *4*, 1759–1764.

[29] a) C. Li, A. Li, Z. Luo, J. Zhang, X. Chang, Z. Huang, T. Wang, J. Gong, *Angew. Chem. Int. Ed.* **2017**, *56*, 4150–4155; b) J. H. Kennedy, and K. W. Frese, *J. Electrochem. Soc.* **1978**, *125*, 709–714.

[30] O. Zandi, A. Agrawal, A. B. Shearer, L. C. Reimnitz, C. J. Dahlman, C. M. Staller, D. J. Milliron, *Nat. Mater.* **2018**, *17*, 710–717.

Entry for the Table of Contents

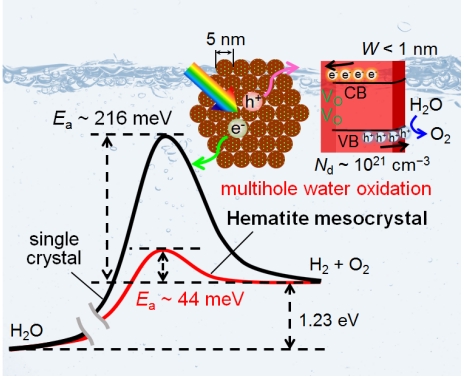

Hematite mesocrystal superstructures with rich interfacial oxygen vacancies yield an exceedingly high carrier density of 4.1×10^{21} cm^{-3} for super bulk conductivity in the electrode and a large quantity of ultra-narrow depletion regions (<1 nm) for high hole collection efficiency, thus boosting multihole water oxidation with a very low activation energy (E_a = 44 meV).